

COORDINATE CHOICE IMPLICATIONS FOR UNCERTAINTY PROPAGATION IN THE CR3BP FRAMEWORK

Sharad Sharan*, Roshan T. Eapen[†], Puneet Singla[‡], Robert G. Melton[§]

This paper employs the conjugate unscented transform technique to accomplish uncertainty propagation using an alternate dynamical model of the Circular Restricted Three Body Problem (CR3BP). The model introduced in this work offers a different perspective to the CR3BP by forging an explicit dependence of the equations of motion on the Jacobi constant. The advantages of such a perspective in constructing the families of periodic orbits and in uncertainty propagation are outlined with examples.

INTRODUCTION

Since the dawn of the Space Age, spacecraft have been sent to inconceivable distances, even far beyond the edges of our Solar System. Space exploration has long since encompassed the cislunar space, however, the prospect of sustained human presence, commercialization and advanced scientific research is only now finding its way from low Earth orbit into cislunar space. Continued expansion in this endeavour is accompanied by various problems, one of them being spacecraft tracking, especially given the enormous distances involved. A chief impediment to spacecraft tracking is uncertainty propagation. It is desirable to be able to predict the spacecraft's state accurately at a later time by propagating the statistical moments of an initial state distribution, so that appropriate information regarding the spacecraft's whereabouts can be passed on to tracking strategies. In order to do this, an appropriate dynamical model is chosen. For cislunar space, this is generally the Circular Restricted Three-Body Problem (CR3BP) with the Earth and the Moon as the primaries.

The CR3BP is a chaotic nonlinear system. Traditional schemes of propagating the central statistical moments rely heavily on linearized dynamics.¹ These schemes are not ideal for a system like the CR3BP. In such cases, a widely used method of uncertainty propagation is the computationally intensive Monte Carlo (MC) method, where tens of thousands of simulations are run for each study.^{2,3} There are several other techniques in literature that use alternate representations of uncertainty, such as the Gaussian mixture approach⁴⁻⁶ and polynomial chaos expansions.^{2,7} Methods like the State Transition Tensor Series (STTS)⁸ replace the MC integrations to generate data for the propagation of moments. However, applying the STTS scheme involves the computation of higher order sensitivities, which is not a trivial process. In this paper, the Conjugate Unscented Transform (CUT)⁹ technique is employed to propagate the central moments. Moreover, CUT is

*Graduate student, Department of Aerospace Engineering, Pennsylvania State University, State College, PA-16802.

[†] Assistant Professor, Department of Aerospace Engineering, Pennsylvania State University, State College, PA-16802.

[‡] Professor, AIAA Associate Fellow, AAS Fellow, Department of Aerospace Engineering, Pennsylvania State University, State College, PA-16802.

[§] Professor, AAS Fellow, AIAA Associate Fellow, Department of Aerospace Engineering, Pennsylvania State University, State College, PA-16802.

shown to compute the higher order sensitivities in a computationally efficient manner, using which the state of each sample in a distribution at any given time can be computed with ease.

Another factor in uncertainty propagation is the way in which the state of the spacecraft is defined.¹ To this effect, a judicious choice of the coordinate system can alleviate many of the challenges in classical uncertainty propagation. A comprehensive theoretical survey of approaches to modeling and representing the restricted three body problem is provided by Szebehely.¹⁰ However, the Cartesian coordinates are widely used, and there has been very minimal numerical exploration using alternative coordinate systems. A coordinate system can be thought of as a language to convey the dynamical messages of a system. Having one universal language to capture and convey the wide variety of dynamics inherent in the CR3BP may not be the best idea for all engineering cases. Therefore, this work explores a modified curvilinear coordinate language consisting of three spherical position coordinates and two velocity pointing angles, to describe the message of uncertainty in the spacecraft's state from an alternate perspective. This curvilinear system is inspired by the reduced order systems elaborated by Szebehely.¹⁰ Propagating an initial Gaussian distribution of the states through the Cartesian CR3BP equations of motion generally leads to a spherical or ellipsoidal distribution. This implies that the uncertainty in velocity vector is defined in all directions. Having the velocity pointing angles themselves as state variables, the uncertainty in velocity vector direction can be defined within a cone, which makes more sense than having it be defined along all directions. This aspect of the proposed model is investigated in this work by applying the computationally inexpensive CUT method to the stochastic analysis of a reference trajectory in the CR3BP.

The organization of the paper is as follows. First, the traditional CR3BP Cartesian model is outlined, following which an alternate five dimensional model of the CR3BP called the Velocity Angles Model (VAM) is discussed. This model ensures constancy of the Jacobi integral, despite numerical precision issues. It is well known that energy preserving integrators are preferred in various fields that involve long-term model propagation,¹¹ like celestial mechanics, plasma physics, and many more. Such problems are modeled as Hamiltonian systems, and symplectic integrators are used to preserve the Hamiltonian throughout the integration. However, symplectic integrators require constraints to be placed in order to hold the Hamiltonian constant, which make the design of such integrators non-trivial. The model presented in this paper requires no such constraints and is independent of the integrator. The Jacobi integral is maintained constant as a result of the way in which the VAM is defined. Building up on the VAM, a spherical model with one radial component and four angular components, referred to as the Spherical-VAM (S-VAM) is developed. A traditional spherical model comprises one radial and two angular components, however, to accomplish the aforementioned goal of maintaining constancy of C , two more angles from the VAM are incorporated to create the S-VAM. Subsequently, the S-VAM is utilized to generate a few families of periodic orbits in the CR3BP, outlining its advantages and drawbacks over the existing Cartesian model. Following this, the S-VAM is employed in quantifying and propagating the uncertainty associated with a reference transfer from a Low Earth Orbit (LEO) to an L_2 halo orbit. The following sections go through the aforementioned contents in detail.

CIRCULAR RESTRICTED THREE BODY PROBLEM

The CR3BP is formulated in a frame that rotates along with the primaries, called the synodic frame. The Earth-Moon synodic frame is illustrated in Figure 1. The \hat{x} basis vector points from the origin, which is at the barycenter of the Earth-Moon system, toward the Moon. The \hat{y} basis

vector is perpendicular to it and lies in the plane of motion of the primaries as shown in Figure 1. The \hat{z} vector is given by the cross product of \hat{x} and \hat{y} . A canonical system of units is employed

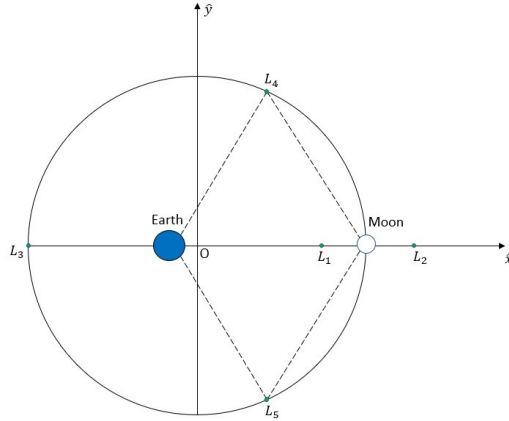


Figure 1: The synodic frame

where one length unit (LU) is equal to the distance between the two primaries and one time unit (TU) is chosen such that the mean motion of the primaries is unity. For the Earth-Moon system, 1 LU = 384 400 km and 1 TU = 4.3424 days.

The Cartesian CR3BP equations of motion are

$$\dot{v}_x = \Omega_x + 2v_y \quad (1a)$$

$$\dot{v}_y = \Omega_y - 2v_x \quad (1b)$$

$$\dot{v}_z = \Omega_z \quad (1c)$$

where $v_x = \dot{x}$, $v_y = \dot{y}$, $v_z = \dot{z}$, and Ω is the pseudo-potential in the synodic frame. Ω_x , Ω_y and Ω_z are the partial derivatives of Ω with respect to x , y and z , respectively.

$$\Omega = \frac{1}{2}(x^2 + y^2) + \frac{(1 - \mu)}{r_1} + \frac{\mu}{r_2} \quad (2)$$

where $r_1 = \sqrt{(x + \mu)^2 + y^2 + z^2}$, $r_2 = \sqrt{(x + \mu - 1)^2 + y^2 + z^2}$, and $\mu = \frac{m_2}{m_1 + m_2}$. r_1 and r_2 are the magnitudes of the position vectors of the spacecraft relative to the Earth and the Moon, respectively. m_1 and m_2 are the masses of the Earth and the Moon, respectively. μ is the characteristic parameter in the synodic frame. For the Earth-Moon system, $\mu = 0.012151$. There exists an integral of motion in the CR3BP known as the Jacobi integral or the Jacobi constant (C).

$$C = 2\Omega - (v_x^2 + v_y^2 + v_z^2) \quad (3)$$

The Jacobi constant is the sole constant of motion in the CR3BP and is a function of the velocity and the pseudo-potential. This model of the CR3BP is the widely used Cartesian model in literature as a good first approximation in the design of cislunar missions. The following section discusses the VAM and how it ensures that C is maintained constant throughout the numerical propagation.

Velocity Angles Model (VAM)

The existence of the Jacobi constant enables a reformulation of the aforementioned 6-dimensional Cartesian model as a 5-dimensional model with Cartesian position components and velocity pointing angles. Such a formulation was used to identify Lyapunov orbits in the Earth-Moon planar CR3BP by Pontani and Conway.¹² A three dimensional extension of that model is developed here. From Fig. 2 and Eq. (3), the following can be written.

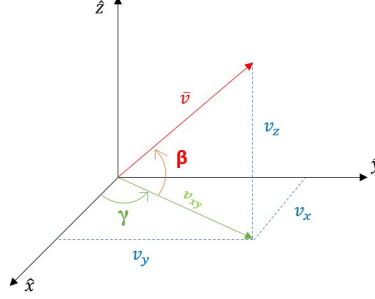


Figure 2: Velocity vector pointing angles

$$v_{xy}^2 = v_x^2 + v_y^2 = 2\Omega - C - v_z^2 \quad (4a)$$

$$v_x = |v_{xy}| \cos \gamma \quad (4b)$$

$$v_y = |v_{xy}| \sin \gamma \quad (4c)$$

$$v_{xy} = |v| \cos \beta \quad (4d)$$

$$v_z = |v| \sin \beta \quad (4e)$$

where γ and β are the velocity pointing angles in the $\hat{x} - \hat{y}$ plane, and out of the $\hat{x} - \hat{y}$ plane, respectively. From Eqs.(4),

$$\tan \gamma = \frac{v_y}{v_x} \quad (5a)$$

$$\tan \beta = \frac{v_z}{v_{xy}} \quad (5b)$$

Differentiating these with respect to time and making appropriate substitutions, expressions for the evolution of γ and β are derived to be

$$\dot{\gamma} = \frac{\Omega_y \cos \gamma - \Omega_x \sin \gamma}{\sqrt{2\Omega - C} \cos \beta} - 2 \quad (6)$$

$$\dot{\beta} = \frac{1}{\sqrt{2\Omega - C}} [\Omega_z \cos \beta - \sin \beta (\Omega_x \cos \gamma + \Omega_y \sin \gamma)] \quad (7)$$

Using Eqs. (6) and (7), the velocity pointing angles can be propagated holding C constant. The fact that C appears explicitly in these equations is what ensures its constancy through the numerical propagation. From these angles, the individual velocity components can be calculated using Eq. (4). Therefore, the VAM ensures that numerical issues do not accumulate error in the Jacobi constant for long term propagations. It is to be noted that when the velocity vector is solely along \hat{z} (i.e., $\beta = \frac{\pi}{2}$),

or when velocity is zero, a singularity is present. However, such a condition was not encountered when dealing with spacecraft approaching or departing periodic orbits in the CR3BP, nevertheless, the possibility exists. Borrowing the velocity pointing angles from the VAM, a curvilinear CR3BP model, the S-VAM is developed in the following section.

S-VAM

Traditionally, a spherical coordinate system includes a radial distance (r), an in-plane angle called the azimuth (θ), and an out-of-plane angle called the elevation (ϕ). In-plane refers to the plane containing all the equilibrium points in the context of the CR3BP. The Cartesian components of position are related to these spherical components in the following way.

$$x = r \cos \phi \cos \theta \quad (8a)$$

$$y = r \cos \phi \sin \theta \quad (8b)$$

$$z = r \sin \phi \quad (8c)$$

The inverse transformation is given by

$$r = \sqrt{x^2 + y^2 + z^2} \quad (9a)$$

$$\theta = \tan^{-1} \left(\frac{y}{x} \right) \quad (9b)$$

$$\phi = \tan^{-1} \left(\frac{z}{\sqrt{x^2 + y^2}} \right) \quad (9c)$$

Eqs.(9) are differentiated with respect to time to obtain the ODEs

$$\dot{r} = \sqrt{2\Omega - C} [\cos \phi \cos \beta \cos(\gamma - \theta) + \sin \phi \sin \beta] \quad (10)$$

$$\dot{\theta} = \frac{\sqrt{2\Omega - C}}{r \cos \phi} \cos \beta \sin(\gamma - \theta) \quad (11)$$

$$\dot{\phi} = \frac{\sqrt{2\Omega - C}}{r} [\sin \beta \cos \phi - \sin \phi \cos \beta \cos(\gamma - \theta)] \quad (12)$$

The Cartesian components in Eqs.(6) and (7) are transformed to the spherical system using Eqs.(9) to obtain

$$\begin{aligned} \dot{\gamma} = \frac{1}{\sqrt{2\Omega - C} \cos \beta} & \left\{ r \cos \phi \sin \theta \cos \gamma \left(1 - \frac{(1 - \mu)}{d_1^3} - \frac{\mu}{d_2^3} \right) \right. \\ & \left. - \sin \gamma \left[r \cos \phi \cos \theta - \frac{(1 - \mu)(r \cos \phi \cos \theta + \mu)}{d_1^3} - \frac{\mu(r \cos \phi \cos \theta - 1 + \mu)}{d_2^3} \right] \right\} - 2 \quad (13) \end{aligned}$$

$$\begin{aligned} \dot{\beta} = \frac{1}{\sqrt{2\Omega - C}} & \left\{ -r \sin \phi \cos \beta \left(\frac{(1 - \mu)}{d_1^3} + \frac{\mu}{d_2^3} \right) \right. \\ & \left. - \cos \gamma \sin \beta \left[r \cos \phi \cos \theta - \frac{(1 - \mu)(r \cos \phi \cos \theta + \mu)}{d_1^3} - \frac{\mu(r \cos \phi \cos \theta - 1 + \mu)}{d_2^3} \right] \right. \\ & \left. - r \cos \phi \sin \theta \sin \gamma \sin \beta \left(1 - \frac{(1 - \mu)}{d_1^3} - \frac{\mu}{d_2^3} \right) \right\} \quad (14) \end{aligned}$$

where,

$$d_1 = \sqrt{r^2 + \mu^2 + 2\mu r \cos \phi \cos \theta} \quad (15a)$$

$$d_2 = \sqrt{r^2 + (\mu - 1)^2 + 2r \cos \phi \cos \theta (\mu - 1)} \quad (15b)$$

Eqs.(10) - (14) can be numerically propagated in the spherical coordinate system, ensuring the preservation of the sole integral of motion, C . It is to be noted that when the velocity is close to zero, a singularity is being approached in the S-VAM: γ and β are no longer uniquely defined. This causes serious deficiencies while analyzing motion in the vicinity of the equilibrium points. Therefore, this model doesn't stand alone as a holistic representation of the dynamics in the CR3BP, instead, it offers an alternative C -oriented perspective to numerical propagation in the CR3BP. In the following section, the VAM and the S-VAM are compared against the Cartesian model.

MODEL VALIDATION

For the purpose of validation, three cases with different initial conditions are chosen in such a way so as to study different parts of the state space. Each trajectory is numerically propagated for a period of 176 days, with an absolute integration tolerance of 10^{-15} .

Case 1

As a first test case, an initial condition is chosen such that the trajectory remains in the vicinity of the Earth for extended periods of time as illustrated in Fig. 3a. This trajectory corresponds to $C = 3.982755396$. The L_1 gateway is closed for this value of C . It can be observed from Fig. 3c, that there is good agreement between the S-VAM and the VAM, both of which preserve C , whereas, the position error between these models and the Cartesian model seems to grow over time. This error is a consequence of the error in C that is accrued by propagation in the Cartesian model, as illustrated in Fig. 3e. However, recall that C is strictly maintained constant in the VAM and S-VAM propagations. Although both VAM and S-VAM results are plotted, recall that the goal here is to explore a fully curvilinear model that preserves C . Since the VAM has rectilinear position components, the main focus in this paper will be on the S-VAM.

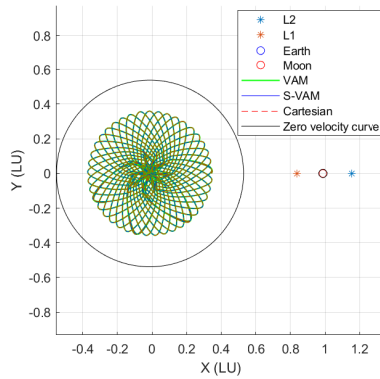
Case 2

In case 2, an initial condition is picked such that the trajectory evolves in the vicinity of the Moon, as illustrated in Fig. 3b. This corresponds to a value of $C = 3.181281559$. Once again, there is a good agreement between the VAM and the S-VAM as seen in Fig. 3d. The error evolution in C follows a similar trend as in Case 1, but in higher magnitudes, as illustrated in Fig. 3f. This indicates that this trajectory's sensitivity to C is relatively higher than case 1. Therefore, for cases 1 and 2, the VAM and S-VAM seem to be more accurate compared to the Cartesian model since C is strictly preserved.

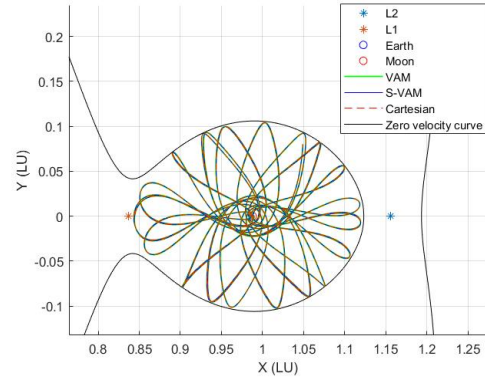
Case 3

After studying the models in the vicinity of the Earth and the Moon in case 1 and case 2, respectively, a trajectory that traverses the L_1 gateway is chosen in case 3. This trajectory corresponds to $C = 3.031508331$. The initial condition is that of a halo orbit, which on long term propagation, leaves the halo and drifts through the L_1 gateway, as illustrated in Fig. 4a. This trajectory is observed to have the most disagreement between the models, among the three cases studied. It

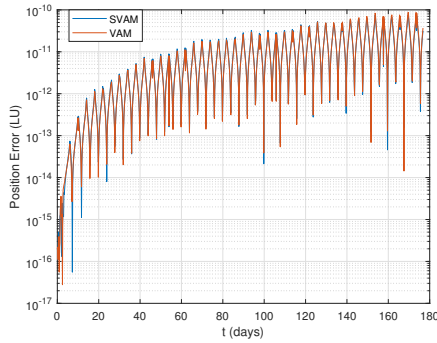
was noted earlier that the VAM and S-VAM were more accurate than the Cartesian model because C was preserved. However, that alone is clearly not the discriminating factor between the models here.



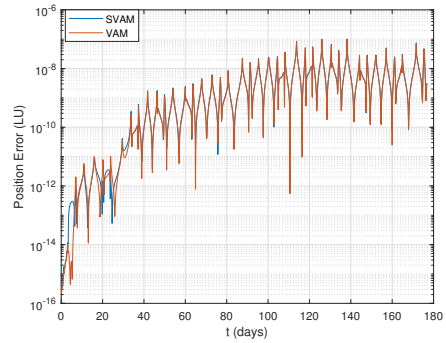
(a) Trajectory (X-Y plane) - Case 1



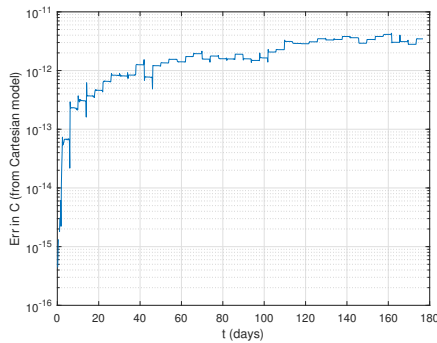
(b) Trajectory (X-Y plane) - Case 2



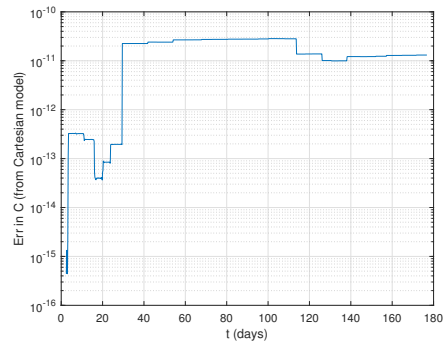
(c) Position error between the Cartesian model and the S-VAM/VAM - Case 1



(d) Position error between the Cartesian model and the S-VAM/VAM - Case 2



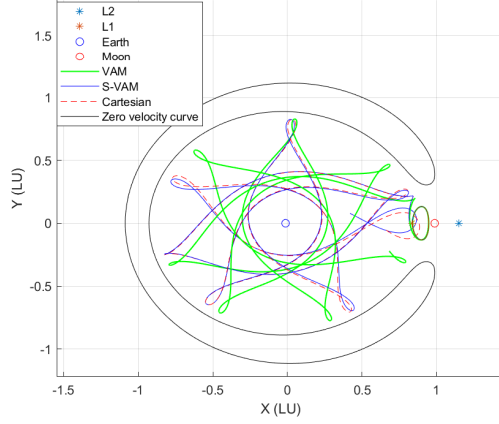
(e) Error evolution in C (Cartesian model) - Case 1



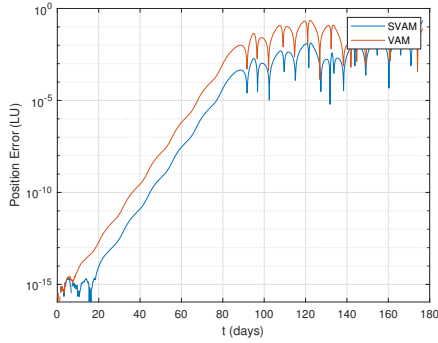
(f) Error evolution in C (Cartesian model) - Case 2

Figure 3: Cases 1 and 2

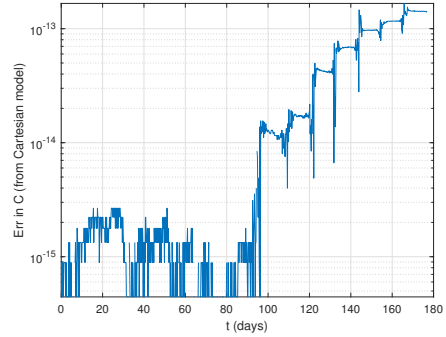
Considering the dynamics modeled by the CR3BP, an initial condition pertaining to a periodic solution must ensure that the solution is maintained as the trajectory is propagated through time.



(a) Trajectory (X-Y plane)



(b) Position error between the Cartesian model and the S-VAM/VAM



(c) Error evolution in C (Cartesian model)

Figure 4: Case 3

The fact that it departs the periodic solution in case 3 indicates the accumulation of numerical errors, as well as the high sensitivity of the CR3BP. Every numerical propagation accrues error. The error observed in C in the Cartesian propagation is due to the errors accumulated in each of the states. Error accumulation is not the same in curvilinear and rectilinear coordinates. Recall that the VAM is partially rectilinear, while the S-VAM is curvilinear. Although both of them preserve the parameter C , errors still accumulate in their states in different ways. These error manifestations are investigated through a parameter sensitivity analysis that is detailed in the following section.

PARAMETER SENSITIVITY ANALYSIS

In order to obtain further insight into the disagreement between the models in case 3, a sensitivity analysis with respect to C can be carried out. In the Cartesian propagation, the variation in C due to the variation in each state variable is computed and plotted in Fig. 5. These plots essentially tell us about the variation in C for a unit variation in the state variables. When these sensitivities are multiplied by an assumed state variation on the order of the integration tolerance, then δC values close to the ones shown in Fig. 4c are observed. It is also observed that the variation in x has the

most profound effect on the variation in C .

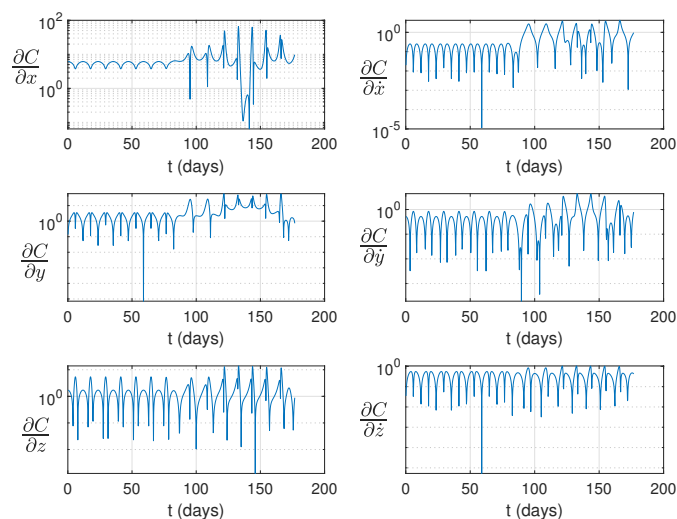


Figure 5: Sensitivity of C with respect to the states

In the S-VAM propagation, C is held constant, therefore there is no variation in C . However, numerical errors have to manifest somewhere else, as they cannot be magically erased by a transformation. Having said that, there is no evidence to the contrary that they cannot be mitigated by a transformation. To that effect, the variation in velocity is studied.

$$\begin{aligned}
 C &= 2\Omega - v^2 \\
 \delta C &= 2\delta\Omega - 2v\delta v \\
 \delta v &= \frac{\delta\Omega}{v}
 \end{aligned}$$

$\delta\Omega$ is in turn a function of r , θ and ϕ . Therefore, the sensitivity of v with respect to r , θ and ϕ are computed and plotted in Fig. 6. It appears that δr is most influential on δv . Following a rough comparison between the largest effects induced on δC and δv , from Figs. 5 and 6, respectively, it can be said that for this particular trajectory, the numerical errors accumulated by the S-VAM (manifesting in velocity) are smaller than those accumulating in the Cartesian model (manifesting in C). The disagreement between the VAM and the S-VAM in Fig. 4b is also explained through this sensitivity analysis, since the error accumulating in x (significantly influences the VAM) is higher than the error accumulating in r which influences the S-VAM. Thus, the S-VAM, with mitigated error accumulation in its curvilinear coordinates and its ability to preserve C , is more accurate, especially for long term propagation, and is adopted as the model of choice for the remainder of this paper. The perspective offered by the S-VAM is further explored by employing it to generate periodic solutions, which is detailed in the following section.

PERIODIC SOLUTIONS USING THE S-VAM

Ideally, the generation of periodic solutions starts with the Lyapunov orbits. These are found using solutions from a linear approximation of the dynamics in the vicinity of a Lagrange point.

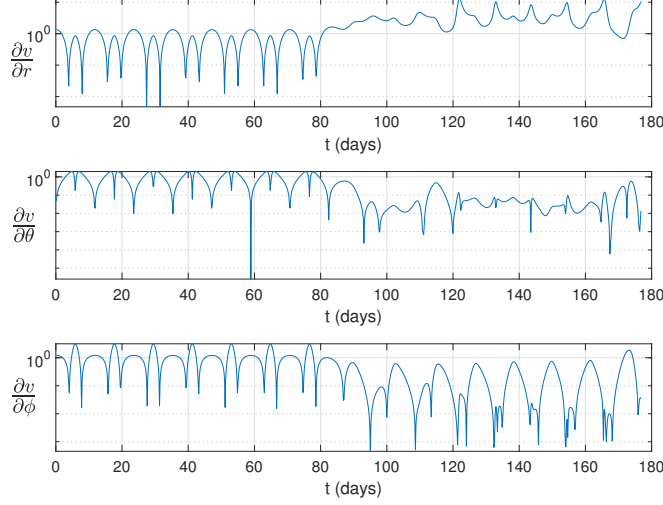


Figure 6: Sensitivity of velocity with respect to position

However, this linearization cannot be performed in the S-VAM due to the singularities at the equilibrium points. The linear approximation for the S-VAM is provided by the Cartesian model to set up the periodic orbit generation process in the S-VAM. Using this approximation, the initial conditions for Lyapunov orbits in the non-linear dynamics are found in the S-VAM by differential correction.

The search for appropriate initial conditions for a periodic orbit starts from the solution to the linear approximation. Thus, an iterative scheme is necessary to take this initial linear approximation, apply it to the nonlinear dynamic system, and correct it until it converges to the required solution. In the Cartesian space, the use of mirror configurations plays a vital role while applying the differential correction scheme to an approximate solution. In a similar fashion, mirror configurations are explored in the S-VAM.

A well known property of the Lyapunov orbit is that it is planar, and crosses the $x - z$ plane perpendicularly. This means that at the crossing, we have a configuration of the state $([r, \theta, \phi, \gamma, \beta])$ that resembles a planar mirror: $[r, 0, 0, \frac{\pi}{2}, 0]$. This knowledge enables us to define the constraints and parameters with which the differential corrector can be set up with. The design variables are the ones the differential corrector is solving for. In this case, they would be r and τ , where τ is the half time period. The constraints at the final time would be $\theta_f = 0$ and $\gamma_f = -\frac{\pi}{2}$. The parameter which is held constant in order to find the design variables is C . The differential correction can now be performed as

$$\begin{bmatrix} r \\ \tau \end{bmatrix}_{new} = \begin{bmatrix} r \\ \tau \end{bmatrix}_{old} - \begin{bmatrix} \Phi_{\theta,r} & \dot{\theta}_f \\ \Phi_{\gamma,r} & \dot{\gamma}_f \end{bmatrix}^{-1} \begin{bmatrix} \theta_f \\ \gamma_f + \frac{\pi}{2} \end{bmatrix} \quad (16)$$

where, Φ is the State Transition Matrix (STM). This process is carried out to obtain an initial condition pertaining to a Lyapunov orbit. Now, the entire family of Lyapunov orbits can be obtained by Natural Parameter Continuation (NPC). This refers to the process by which the parameter (C in

this case) is stepped up or down by a certain amount, and the initial conditions corresponding to the new value of the parameter are found by iteratively solving Eqn.(16). This process was carried out to obtain the L_1 and L_2 families of Lyapunov orbits as illustrated in Fig. 7a. It is to be noted that in computing these families, a total of 30 ODEs were integrated in the S-VAM to get the states and the STM, as opposed to integrating 42 ODEs in the regular Cartesian model, thereby significantly reducing computation.

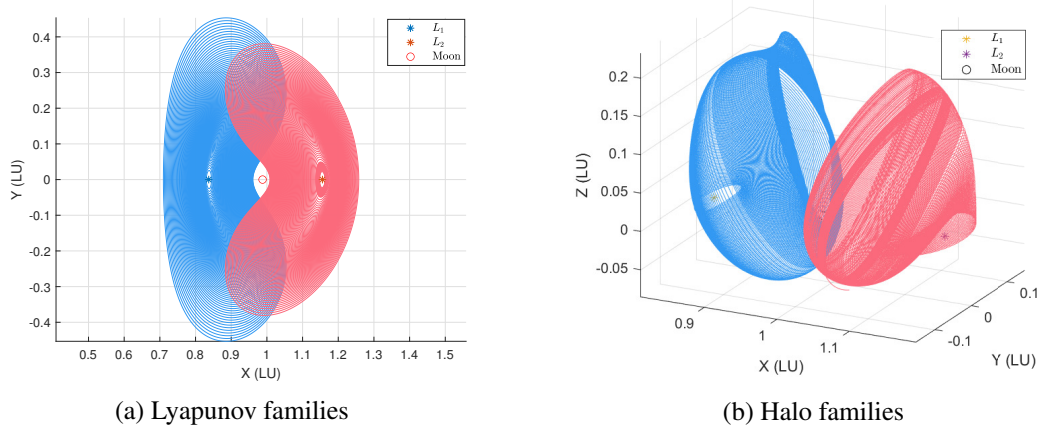


Figure 7: Periodic orbits generated using the S-VAM

In order to identify halo orbits, we look for a configuration of the state resembling a reflection $([r, 0, \phi, \frac{\pi}{2}, 0])$ at the $x - z$ crossing. Unlike the Lyapunov orbit generation, C cannot be used for the NPC here. This is because, C as a parameter, does not force the corrector to look for initial conditions out of the plane. The only state forcing that is ϕ . Therefore, ϕ must be used as a parameter to ensure that the corrector doesn't find planar Lyapunovs again. The correction process is now carried out as

$$\begin{bmatrix} r \\ C \\ \tau \end{bmatrix}_{new} = \begin{bmatrix} r \\ C \\ \tau \end{bmatrix}_{old} - \begin{bmatrix} \Phi_{\theta,r} & \Phi_{\theta,C} & \dot{\theta}_f \\ \Phi_{\gamma,r} & \Phi_{\gamma,C} & \dot{\gamma}_f \\ \Phi_{\beta,r} & \Phi_{\beta,C} & \dot{\beta}_f \end{bmatrix}^{-1} \begin{bmatrix} \theta_f \\ \gamma_f + \frac{\pi}{2} \\ \beta_f \end{bmatrix} \quad (17)$$

Notice that while applying Eqn.(17), the STM should also include the partial derivatives of the states with respect to C . This means an additional dummy equation of motion $\dot{C} = 0$ is included, thereby bringing the system order back to 6. This is done solely for the purpose of finding the sensitivities of the states to C . On carrying out the NPC along ϕ , a family of halos is obtained as illustrated in Fig. 7b. NPC is subsequently carried out along r to obtain more members of the family. The generation of periodic solutions completes a comprehensive testing of the S-VAM in the natural dynamics of the CR3BP. The following section explores uncertainty propagation using the S-VAM, its advantages and limitations in detail.

UNCERTAINTY PROPAGATION

Uncertainty propagation in the S-VAM is carried out using the Conjugate Unscented Transform (CUT)⁹ technique. It is an extended form of the unscented transform (UT), with modifications in

the definition of the traditional sigma points. UT and CUT fall under a category of non-product quadrature schemes. To begin discussion on these schemes, a quick recap of basic quadrature schemes is presented here. The fundamental idea behind any quadrature scheme is that the integral of a function can be expressed as a weighted sum of function evaluations at specific points. These points and weights are what differentiate the various quadrature methods. Applying this idea to find the expectation value of $f(x)$,

$$E[f(x)] = \sum_{i=1}^N w_i f(x_i) \quad (18)$$

where x_i are the specific points where the function is evaluated, w_i are the corresponding weights assigned and N is the total number of points. Note that in a multidimensional system, f and x are both vectors. Expressing $f(x)$ as a Taylor series of m^{th} order about a nominal solution (x^*),

$$f(x) = f(x^*) + \frac{\partial f(x^*)}{\partial x_{\alpha_1}} \delta x_{\alpha_1} + \dots + \frac{1}{m!} \frac{\partial^m f(x^*)}{\partial x_{\alpha_1} \dots \partial x_{\alpha_m}} \delta x_{\alpha_1} \dots \delta x_{\alpha_m} \quad (19)$$

for $\alpha_1, \dots, \alpha_m = 1, \dots, n$, where n is the number of dimensions. Substituting Eq. (19) in Eq. (18), and noting that the partial derivatives are constants, we get

$$\begin{aligned} & f(x^*) + \frac{\partial f(x^*)}{\partial x_{\alpha_1}} E[\delta x_{\alpha_1}] + \frac{1}{m!} \frac{\partial^m f(x^*)}{\partial x_{\alpha_1} \dots \partial x_{\alpha_m}} E[\delta x_{\alpha_1} \dots \delta x_{\alpha_m}] \\ &= f(x^*) \sum_{i=1}^N w_i + \frac{\partial f(x^*)}{\partial x_{\alpha_1}} \sum_{i=1}^N w_i \delta x_{\alpha_1}^{(i)} + \dots + \frac{1}{m!} \frac{\partial^m f(x^*)}{\partial x_{\alpha_1} \dots \partial x_{\alpha_m}} \sum_{i=1}^N w_i \delta x_{\alpha_1}^{(i)} \dots \delta x_{\alpha_m}^{(i)} \end{aligned} \quad (20)$$

Equating the coefficients of the partial derivatives on both sides of Eq. (20) yields the Moment Constraint Equations (MCEs)

$$E[\delta x_{\alpha_1}] = \sum_{i=1}^N w_i \delta x_{\alpha_1}^{(i)} \quad (21)$$

$$E[\delta x_{\alpha_1} \delta x_{\alpha_2}] = \sum_{i=1}^N w_i \delta x_{\alpha_1}^{(i)} \delta x_{\alpha_2}^{(i)} \quad (22)$$

⋮

$$E[\delta x_{\alpha_1} \dots \delta x_{\alpha_m}] = \sum_{i=1}^N w_i \delta x_{\alpha_1}^{(i)} \dots \delta x_{\alpha_m}^{(i)} \quad (23)$$

Therefore, given the knowledge of these expectation values (statistical moments) of x , the moments of $f(x)$ can be evaluated up to m^{th} order accuracy by solving for a specific set of points and corresponding weights, such that the MCEs are satisfied.¹³

The traditional method of finding the statistical moments is the Monte Carlo (MC) method. Several points from an initial probability density function are selected and propagated through the nonlinear system dynamics to evaluate the statistical moments at the final time. This scheme of random sampling means that the MCEs are approximately satisfied as the number of sampled points increases, but never exactly satisfied.

Deterministic techniques to satisfy these constraints are generally provided by various quadrature methods, the most renowned being the Gaussian Quadrature Rule (GQR). GQR provides the minimum number of points necessary to satisfy the MCEs when dealing with a single variable. N points are necessary to integrate up to $(2N - 1)^{th}$ order polynomials.¹⁴ The addition of dimensions brings with it the need to construct a grid of quadrature points by computing tensor products of the one dimensional points, therefore leading to an exponential growth in the required number of points, consequently increasing computational costs.

Sparse grid methods¹⁵⁻¹⁷ are well known alternatives to GQR, since they require fewer points compared to full tensor product methods. However, the sparse tensor product scheme is prone to cause negative weights, which allow significant error to creep into the integration.¹³ Thus enter non-product quadrature schemes.

The UT is a popular non-product quadrature method. UT is capable of integrating n-dimensional variables up to third-order accuracy with simply a linear growth in the number of required points.¹⁸ The points are placed symmetrically on the principal axes of the n-dimensional variables. Due to this symmetry, all odd-order moments are inherently satisfied. The even-order moments are then used to solve for the exact position of these points and their weights. A drawback of the UT is that any moment that includes more than one dimension cannot be satisfied by simply placing points on the principal axes. This is where the CUT method takes over.

The CUT is similar to UT in that it has points placed symmetrically on the principal axes such that odd-order moments are automatically satisfied. In addition to these axes, a conjugate set of axes is also defined, which contain several symmetrically placed points as well. These points along the conjugate axes help satisfy the cross-moment constraints in the case of multidimensional variables.¹⁹ Altogether, the CUT points ensure the exact evaluation of multidimensional expectation integrals with a significantly smaller number of points than the previously discussed schemes. Adurthi et al.¹⁹⁻²² provide an extensive study with applications outlining the advantages of the CUT methodology over conventional quadrature rules. Adopting the CUT method, stochastic study of a reference trajectory in the CR3BP is carried out using the S-VAM in the following section.

Case study

In order to test uncertainty propagation in the S-VAM, a reference transfer from a low Earth orbit to an L_2 halo orbit is chosen, as illustrated in Fig. 8. An impulsive ΔV is applied to this translunar trajectory to effect insertion into a trajectory on the stable manifold of the halo orbit. It is to be noted that due to the nature of the S-VAM, uncertainty in the magnitude of the velocity vector can be dealt with, independent of the uncertainty in its direction. The following study deals with the uncertainty associated with the firing angle of the thruster, and the position of the spacecraft at the impulse point. In order to capture this uncertainty, a uniform distribution of samples corresponding to $\pm[5 \text{ km}, 0.2^\circ, 0.2^\circ, 5^\circ, 5^\circ]$ in $[r, \theta, \phi, \gamma, \beta]$ about the impulse point on the reference trajectory is generated. Note that this setup assumes that the energy imparted by the thruster is same as that of the reference transfer. First, 1 000 000 Monte Carlo samples are integrated for a time period of two days using the S-VAM. This is followed by multiple sets of simulations, that are carried out by subsequently reducing the number of samples by an order of ten.

The first and second order statistical moments are calculated for each set of MC simulations, and compared with those obtained using the CUT methodology. The two norm of the error in the mean and covariance between the two methods is plotted as illustrated in Fig. 9. It can be observed that

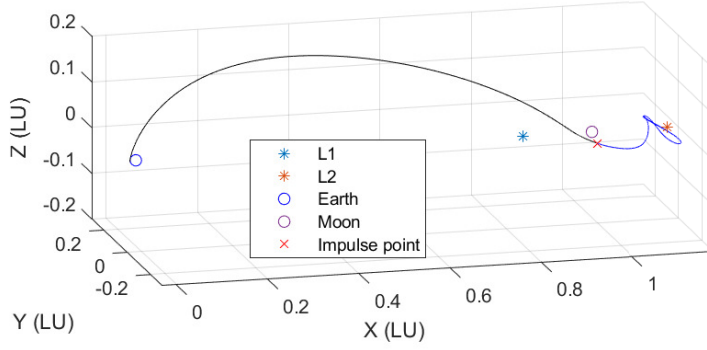


Figure 8: Reference trajectory from LEO to an L_2 halo orbit

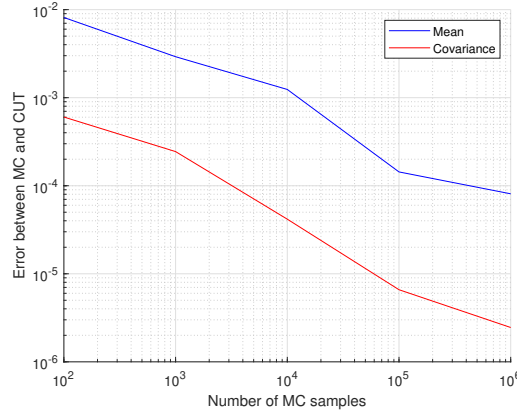


Figure 9: Two-norm error between the CUT and MC computations of the mean and covariance

as the number of samples increases, the error between MC and CUT reduce. This is indicative of the fact that the CUT points enable an accurate calculation of the moments without the need for numerous samples like the MC method. In addition to being able to compute the statistical moments in a computationally efficient manner, CUT can also be used to approximate the solution flow.

Approximating the solution flow: Earlier, the approximation of a function by means of a Taylor series about a reference value of the function was discussed. Revisiting that, Eq. (19) can be written compactly as

$$\mathbf{f}(\mathbf{x}) \approx D\Phi(\mathbf{x}) \quad (24)$$

where D is a matrix of coefficients corresponding to the partial derivatives, and $\Phi(x)$ is a vector of polynomial basis functions. In computing the solution flow, evaluation of the partial derivatives to build the D matrix is generally the computationally expensive part. However, if $f(x)$ and $\Phi(x)$ were known, it would only take a least squares procedure to evaluate D , as opposed to going through cumbersome integration to find the partials. Due to the aforementioned advantages, the CUT points are chosen as the points at which $f(x)$ and $\Phi(x)$ are evaluated.

The approximation error is given by

$$e_j = f_j(x) - d_{ji}\Phi_i(x) \quad (25)$$

The cost function to minimize is

$$J = \frac{1}{2} \langle e_j, e_j \rangle \quad (26)$$

The inner product is with respect to the weights assigned to the CUT points. Minimizing J ,

$$\frac{\partial J}{\partial d_{jk}} = 0 \quad (27)$$

$$\Rightarrow \langle f_j(x), \Phi_k(x) \rangle = d_{ji} \langle \Phi_i(x), \Phi_k(x) \rangle \quad (28)$$

$$d_{ji} = \frac{\langle f_j(x), \Phi_k(x) \rangle}{\langle \Phi_i(x), \Phi_k(x) \rangle} \quad (29)$$

However, given a set of orthogonal polynomial basis functions, we can say that

$$\langle \Phi_i(x), \Phi_k(x) \rangle = 0, \text{ for } i \neq k \quad (30)$$

This further reduces computational complexity, as the matrix of the inner products of these orthogonal polynomials (the normal matrix) is diagonal. Computing the inverse of a diagonal matrix is trivial, therefore, basis functions are preferred to be orthogonal. In addition to this, the normal matrix can be computed offline, thereby reducing on-the-fly computational load. In this work, the orthogonal polynomial basis functions up to degree four are considered. As a result of making $\phi_i(x)$ orthogonal, the coefficients computed are not exactly a reflection of the partial derivatives that appear in the Taylor series, nevertheless, they carry the same notion of sensitivities in the new basis system.

Altogether, evaluation of $f(x)$ and $\phi(x)$ at the CUT points enable the computation of the sensitivity coefficients (matrix D). D can then be used to approximate the solution at any point in the vicinity of the reference trajectory as $D\Phi(\zeta)$, where ζ is the state vector normalized in accordance with the distribution of CUT points chosen to evaluate the basis functions at. In this way, the solution at the final time for all the samples can be found using the sensitivity coefficients. This is referred to as the sensitivity matrix method (SMM).¹³ The SMM is extremely useful, as it allows a significantly quicker function evaluation, as opposed to a series of integration using an MC scheme. This can be realized by clocking the computation time for each method, as shown in Table 1. All computations were run on an Intel Xeon E5-2695 processor and parallelized over 32 cores. There is no parallelization necessary while using the CUT scheme.

Number of samples	Computation time (MC) (sec)	Computation time (CUT) (sec)
1 000 000	507.06	9.43
100 000	80.41	0.84

Table 1: Comparison of computation time

In order to learn the accuracy of the SMM approximation, the two norm of the error in position is plotted against the initial and final Mahalanobis distances of the samples, as shown in Fig. 11. The Mahalanobis distance (M_d) of each sample is calculated as

$$M_d = \sqrt{(\vec{x}_t - \vec{\mu}_t)^T \Sigma_t^{-1} (\vec{x}_t - \vec{\mu}_t)} \quad (31)$$

where μ_t is the mean vector of the state distribution at time t , and Σ_t is the covariance of the distribution. M_d is a measure of how far the multi-dimensional sample sits from the mean. Three different cases are studied, with each case differing by the degree of uncertainty in the velocity pointing angles, as summarized in Table 2 and illustrated in Fig. 10. It can be discerned from the cones of uncertainty in Fig. 10, that changes in the velocity vector direction inside the cone could possibly take the spacecraft away from the intended terminal manifold. Even worse, if the spacecraft has enough energy to reach the family of halos around L_2 and it is not heading the right way, then that energy level is sufficient to carry the spacecraft through the L_2 gateway and out of the system. Therefore, such a sensitive trajectory is chosen as the test case for our stochastic analysis. Uncertainty in the position of the spacecraft during the impulse is taken to be $\pm[5 \text{ km}, 0.2^\circ, 0.2^\circ]$ about the reference impulse point for all the cases.

	γ (deg)	β (deg)
Case 1	$[-5, 5]$	$[-5, 5]$
Case 2	$[-10, 10]$	$[-10, 10]$
Case 3	$[-15, 15]$	$[-15, 15]$

Table 2: Assumed range of deviation of the samples from the reference impulse point

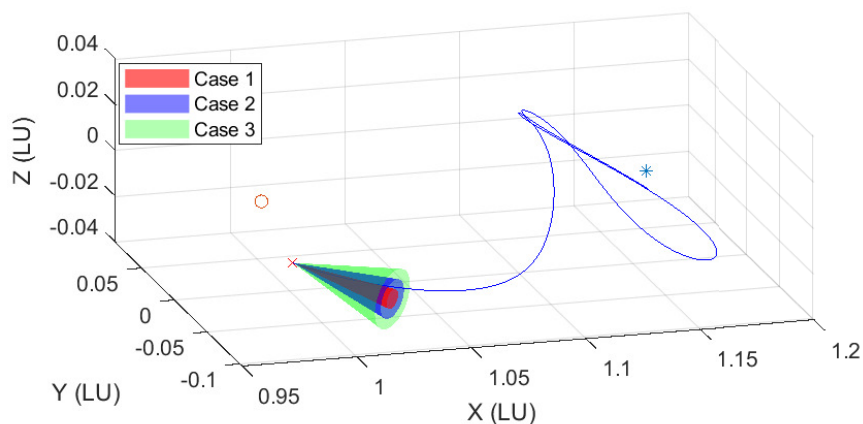


Figure 10: Cone of uncertainty (γ, β)

The time at the impulse point is designated as t_0 , and the time of propagation of the samples is designated as t_f . M_d is calculated for the samples at t_0 and t_f and plotted along the x and y axes, respectively, in Fig. 11. The colorbar is representative of the position error in km between the MC integration and the CUT approximation. Figs. 11a, 11b and 11c provide information about the distributions in the three cases 30 min after the impulse. The maximum position error for case 1 at this t_f is on the order of 10^{-3} km. As the initial range of uncertainty in γ and β increases in cases 2 and 3, the errors creep up as well. A diagonal structure in Fig. 11a indicates that the samples which start off at a specific M_d at t_0 retain more or less the same M_d at t_f . However, it can quickly be seen that this structure does not last with increase in t_f , as illustrated in Figs. 11d and 11g for case 1. At $t_f = 52$ hours, the maximum error for case 1 is on the order of hundreds of meters, thus reaching a threshold beyond which the CUT approximation is no longer valid.

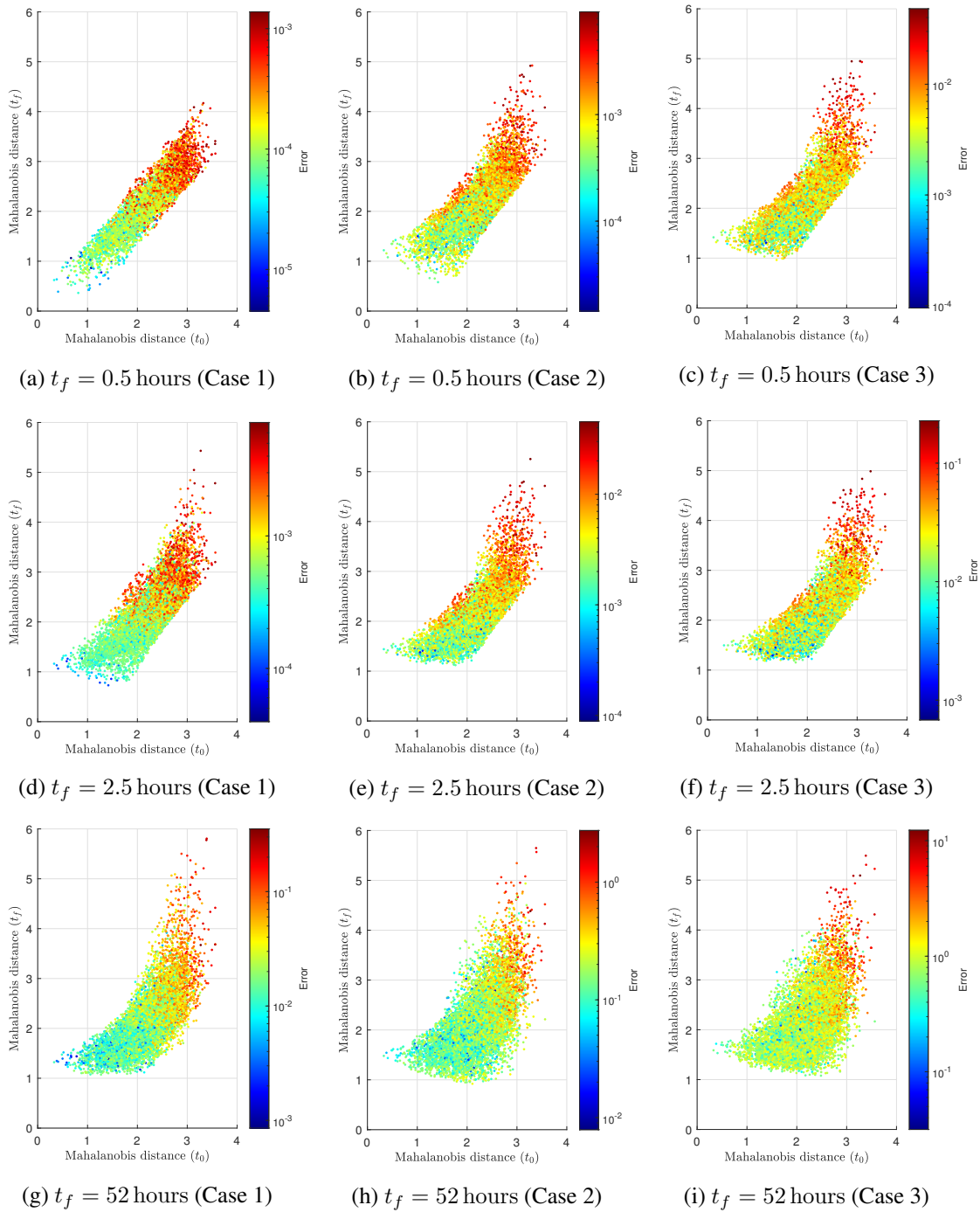


Figure 11: Position error (in km) between MC integration and CUT approximation plotted against the initial and final Mahalanobis distances of the samples

Recall that case 1 had the lowest maximum deviation in γ and β . This indicates that for this particular trajectory, uncertainty can be propagated at a significantly reduced computational cost for up to 50 hours using CUT, should the initial deviation in γ and β be less than 5° . As this initial

deviation increases, the time of validity of the CUT approximation decreases, as illustrated in the plots corresponding to cases 2 and 3 in Fig. 11. The CUT approximation is considered valid in these simulations, as long as the maximum error is on the order of 10^{-2} km. It is clear from Figs. 11h and 11i, that γ and β samples belonging to the cones of uncertainty corresponding to cases 2 and 3, carry very high errors on the order of kilometers after 52 hours. Therefore, CUT can no longer be used and a more tedious MC scheme is required. However, in a practical sense, we would not require the propagation of uncertainty for over two days, as the frequency of observation would be higher than one in two days.

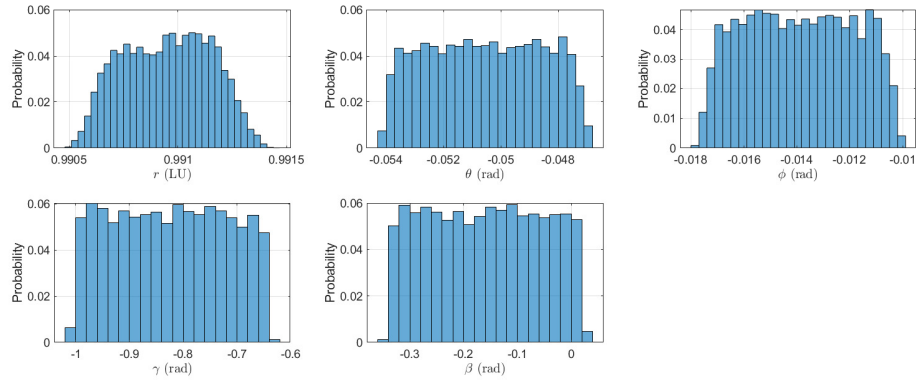
After having gauged the degree of accuracy of the SMM, it can now be used to obtain stochastic insight that will aid not only in the trajectory planning, but also the tracking process. It would be beneficial to know the consequences of an off-nominal burn at a later time, so that the sensors can be tasked to re-acquire the spacecraft at the next instance of observation. In order to do that, useful information can be gathered from histograms of the states, which are illustrated in Fig. 12 for case 1. At $t_f = 0.5$ hours, the distribution is more or less rectangular (Fig. 12a), consistent with our construction of initial samples which were uniformly distributed. As t_f increases, the probabilities vary as illustrated in Figs. 12b and 12c, providing information on the best estimate of the spacecraft's state at any given time. Using this, sensors can be tasked to achieve a successful observation. The SMM, with its significantly low computational expense, allows such an analysis to be possible, much quicker than a traditional MC routine. Moreover, for this case study of a misfired thruster, the S-VAM, being a reduced order model, offers further reduction in computation required by the SMM.

SUMMARY

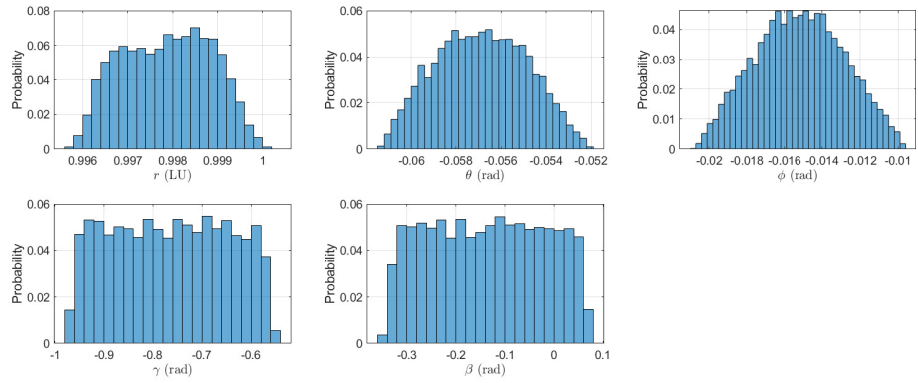
An alternate five dimensional model of the CR3BP, called the S-VAM was derived. This model was tested in multiple different regimes of the CR3BP. The S-VAM raised a question of "which model is closer to the truth?", which led to a sensitivity analysis that yielded further insight about the nature in which the states and parameters of the system are interwoven. During the model validation phase, three trajectories were propagated for a period of 176 days. Such a period is well within the ballpark of a low-thrust spacecraft traversing cislunar space.²³ The aforementioned sensitivity analysis was carried out for this entire period on one of the trajectories. This analysis concluded that the S-VAM accumulated smaller numerical errors compared to the Cartesian model, with the added advantage of preserving C throughout the integration. This renders long-term propagation using the S-VAM more reliable than the Cartesian system. Therefore, the S-VAM proves to be the model of choice for analysis of low-thrust spacecraft trajectories in cislunar space. Following this, it was successfully demonstrated that Lyapunov and halo orbits can be generated in the S-VAM, with increased computational advantage over the traditional Cartesian system.

The S-VAM enabled the propagation of uncertainty in the direction of velocity, independent of its magnitude. A case study was presented to illustrate this feature. The SMM, using CUT points in the S-VAM, was employed to approximate the solution flow about a reference trajectory. The computational significance of the SMM was illustrated by computing the solution flow for a million samples in a meager amount of time compared to the MC approach.

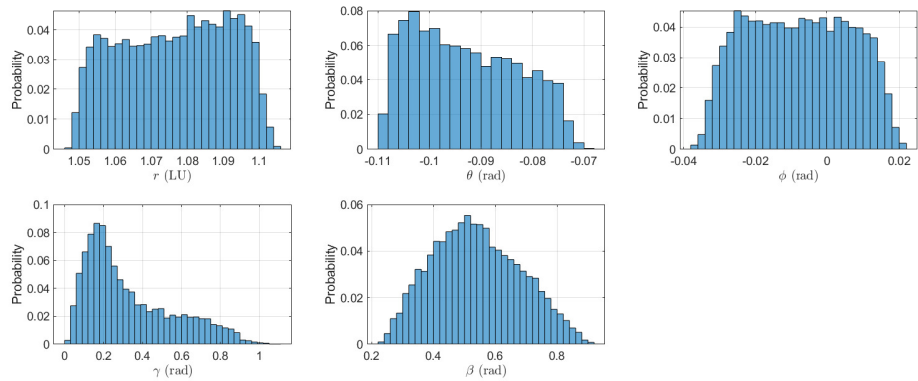
The S-VAM in its present form applies only to a conservative environment. In this work, the S-VAM was employed for stochastic analysis only after the action of the thruster. A continuation of this work will involve modifications to the EOMs such that a non-conservative effect can be included, which will facilitate stochastic analysis of actively maneuvering spacecraft.



(a) $t_f = 0.5$ hours



(b) $t_f = 2.5$ hours



(c) $t_f = 52$ hours

Figure 12: Histograms of the states at different times (Case 1)

ACKNOWLEDGEMENT

This material is based upon work supported jointly by the AFOSR grants FA9550-20-1-0176 and FA9550-22-1-0092.

REFERENCES

- [1] C. Frueh, K. Howell, K. DeMars, and S. Bhadauria, "Cislunar Space Situational Awareness," *31st AIAA/AAS Space Flight Mechanics Meeting*, 2021.
- [2] V. Vittaldev, R. P. Russell, and R. Linares, "Spacecraft uncertainty propagation using Gaussian mixture models and polynomial chaos expansions," *Journal of Guidance, Control, and Dynamics*, Vol. 39, No. 12, 2016, pp. 2615–2626.
- [3] C. Sabol, C. Binz, A. Segerman, K. Roe, and P. W. Schumacher Jr, "Probability of collision with special perturbations dynamics using the monte carlo method," *AAS/AIAA Astrodynamics Specialist Conference, Girdwood, AK*, 2011.
- [4] K. J. DeMars, R. H. Bishop, and M. K. Jah, "Entropy-based approach for uncertainty propagation of nonlinear dynamical systems," *Journal of Guidance, Control, and Dynamics*, Vol. 36, No. 4, 2013, pp. 1047–1057.
- [5] K. Vishwajeet, P. Singla, and M. Jah, "Nonlinear uncertainty propagation for perturbed two-body orbits," *Journal of Guidance, Control, and Dynamics*, Vol. 37, No. 5, 2014, pp. 1415–1425.
- [6] K. J. DeMars, Y. Cheng, and M. K. Jah, "Collision probability with gaussian mixture orbit uncertainty," *Journal of Guidance, Control, and Dynamics*, Vol. 37, No. 3, 2014, pp. 979–985.
- [7] G. Terejanu, P. Singla, T. Singh, and P. D. Scott, "Uncertainty propagation for nonlinear dynamic systems using Gaussian mixture models," *Journal of guidance, control, and dynamics*, Vol. 31, No. 6, 2008, pp. 1623–1633.
- [8] A. B. Younes, J. Turner, M. Majji, and J. Junkins, "High-Order Uncertainty Propagation Using State Transition Tensor Series," *Jer-Nan Juang Astrodynamics Symposium, Univelt, Inc., San Diego, CA, No. AAS*, 2012, pp. 12–636.
- [9] N. Adurthi, P. Singla, and M. Majji, "Conjugate Unscented Transform based approach for dynamic sensor tasking and Space Situational Awareness," *2015 American Control Conference (ACC)*, IEEE, 2015, pp. 5218–5223.
- [10] V. Szebehely, *Theory of orbit: The restricted problem of three Bodies*. Elsevier, 2012.
- [11] H. Qin and X. Guan, "Variational symplectic integrator for long-time simulations of the guiding-center motion of charged particles in general magnetic fields," *Physical review letters*, Vol. 100, No. 3, 2008, p. 035006.
- [12] M. Pontani and B. Conway, "Particle swarm optimization applied to space trajectories," *Journal of Guidance, Control, and Dynamics*, Vol. 33, No. 5, 2010, pp. 1429–1441.
- [13] Z. Hall and P. Singla, "A probabilistic approach for reachability set computation for efficient space situational awareness," *29th AAS/AIAA Space Flight Mechanics Meeting, 2019*, Univelt Inc., 2019, pp. 3001–3020.
- [14] G. H. Golub and J. H. Welsch, "Calculation of Gauss quadrature rules," *Mathematics of computation*, Vol. 23, No. 106, 1969, pp. 221–230.
- [15] T. Gerstner and M. Griebel, "Numerical integration using sparse grids," *Numerical algorithms*, Vol. 18, No. 3, 1998, pp. 209–232.
- [16] F. Heiss and V. Winschel, "Likelihood approximation by numerical integration on sparse grids," *journal of Econometrics*, Vol. 144, No. 1, 2008, pp. 62–80.
- [17] B. Jia, M. Xin, and Y. Cheng, "Sparse-grid quadrature nonlinear filtering," *Automatica*, Vol. 48, No. 2, 2012, pp. 327–341.
- [18] S. Julier, J. Uhlmann, and H. F. Durrant-Whyte, "A new method for the nonlinear transformation of means and covariances in filters and estimators," *IEEE Transactions on automatic control*, Vol. 45, No. 3, 2000, pp. 477–482.
- [19] N. Adurthi, P. Singla, and T. Singh, "Conjugate unscented transform and its application to filtering and stochastic integral calculation," *AIAA Guidance, Navigation, and Control Conference*, 2012, p. 4934.
- [20] N. Adurthi, P. Singla, and T. Singh, "The conjugate unscented transform—an approach to evaluate multi-dimensional expectation integrals," *2012 American Control Conference (ACC)*, IEEE, 2012, pp. 5556–5561.
- [21] N. Adurthi and P. Singla, "Conjugate unscented transformation-based approach for accurate conjunction analysis," *Journal of Guidance, Control, and Dynamics*, Vol. 38, No. 9, 2015, pp. 1642–1658.
- [22] N. Adurthi, P. Singla, and T. Singh, "Conjugate unscented transformation: Applications to estimation and control," *Journal of Dynamic Systems, Measurement, and Control*, Vol. 140, No. 3, 2018.
- [23] S. Sharan and R. G. Melton, "Design of low thrust trajectories from low earth orbit to distant retrograde orbits by particle swarm optimization," *AAS/AIAA Astrodynamics Specialist Conference, 2020*, Univelt Inc., 2021, pp. 4561–4579.